Geophysical Research Letters

RESEARCH LETTER
10.1029/2023GL105150

Thermally Direct Mesoscale Circulations Caused by Land Surface Roughness Anomalies

Yu Cheng[1] **and Kaighin A. McColl**[1,2]

[1]Department of Earth and Planetary Sciences, Harvard University, Cambridge, MA, USA, [2]School of Engineering and Applied Sciences, Harvard University, Cambridge, MA, USA

Key Points:

- Land surface roughness anomalies caused by human activities can induce changes in climate
- Anomalously high roughness leads to greater sensible heat flux, triggering mesoscale circulations and precipitation
- This new mechanism may be relevant to storm formation over wind farms, cities and forests

Supporting Information:

Supporting Information may be found in the online version of this article.

Correspondence to:

K. A. McColl,
kmccoll@seas.harvard.edu

Citation:

Cheng, Y., & McColl, K. A. (2023). Thermally direct mesoscale circulations caused by land surface roughness anomalies. *Geophysical Research Letters*, *50*, e2023GL105150. https://doi.org/10.1029/2023GL105150

Received 26 JUN 2023
Accepted 4 AUG 2023

Abstract Deforestation, urbanization and construction of wind farms can change the land surface roughness, which can further influence surface heat fluxes and thus weather and climate. Land surface roughness anomalies can dynamically trigger convergence through changing mean wind speed. Here, we report a new mechanism, in which roughness anomalies cause thermally direct mesoscale circulations and anomalous precipitation. To study this mechanism, we conduct cloud-permitting simulations over an idealized land surface with prescribed surface roughness anomalies. Anomalously high roughness increases turbulent mixing near the surface, which decreases land surface temperature and outgoing longwave radiation. The additional surface net radiation partly goes into greater sensible heat flux, which triggers mesoscale circulations driven by differential heating. As a result, precipitation over the high-roughness anomaly is generally larger than that over the low-roughness background. This new mechanism, not present in climate models, may be relevant to storm formation over wind farms, cities and forests.

Plain Language Summary The Earth's surface roughness determines the turbulent exchange efficiency of momentum, heat, water vapor, and carbon dioxide between the atmosphere and surface, and thus serves as a key boundary condition for predicting weather and climate. Surface roughness can be modified by human activities, such as deforestation, urbanization, and construction of wind farms. It is recognized that land surface roughness anomalies can dynamically trigger convergence and precipitation anomalies through changing mean wind speed. Compared to its dynamical effects, the thermal effects of roughness anomalies have largely been overlooked. In this study, we report that higher roughness can lead to thermally direct mesoscale circulations and more precipitation. This new mechanism, neglected in previous coarse-resolution climate models, could be significant for predicting storms over wind farms, cities, and forests.

1. Introduction

Land surface modifications like deforestation, urbanization and construction of wind farms can change the surface roughness, which further influences turbulent exchange of momentum, heat, water vapor, and carbon dioxide between the atmosphere and the Earth's surface (Deardorff, 1972; Louis, 1979). At synoptic scales (O(1,000 km)), roughness anomalies caused by wind farms can trigger Rossby waves and induce anomalies in wind, temperature, and cloud cover (Kirk-Davidoff & Keith, 2008). At mesoscales (O(10 km)), changes in roughness caused by deforestation can generate "dynamically driven" mesoscale circulations (Khanna & Medvigy, 2014; Samuelsson & Tjernström, 2001), which are essentially horizontal divergence or convergence due to the speed change of mean horizontal winds over different roughness surfaces.

In contrast to the dynamically driven mesoscale circulations reported in previous studies (Khanna & Medvigy, 2014; Samuelsson & Tjernström, 2001), here we report a new mechanism: "thermally direct" mesoscale circulations caused by differential heating that arises in the presence of roughness anomalies. How can an anomaly in roughness cause anomalous heating? Consider a deliberately extreme, idealized example, used here to qualitatively illustrate the mechanism. An otherwise uniform domain is divided into two regions, one rough (denoted with "R" subscripts) and one perfectly smooth (denoted with "S" subscripts). In this idealized example, the roughness of the surface entirely controls the intensity of turbulent mixing near the surface, encoded in the "aerodynamic conductance" parameter (g_a), and the aerodynamic conductance of the smooth region is zero.

As detailed in Supporting Information S1, the heating differential between the rough and smooth regions is

$$\Delta H \equiv H_R - H_S = H_R \quad (1)$$

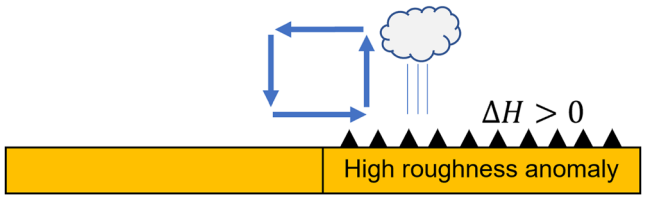

Figure 1. Schematic of mesoscale circulations generated by differential heating due to a roughness anomaly.

where H is the sensible heat flux. This example shows that a surface roughness anomaly is capable of causing an anomaly in sensible heat flux, solely due to basic constraints imposed by the surface energy budget. Moreover, over land, the sensible heat flux is typically positive during the day outside high latitudes, and also in the daily, monthly and annual means. This implies that ΔH is typically positive, and rough anomalies should heat the atmosphere more than their smoother surroundings, potentially triggering mesoscale circulations and precipitation (Figure 1).

These arguments are based on a deliberately simple and idealized model in which the region surrounding the rough anomaly is perfectly smooth with zero turbulent fluxes. Does the mechanism persist in less extreme cases? And, are the heating anomalies sufficient to trigger mesoscale circulations that cause precipitation? To answer these questions, we turn to cloud-permitting simulations.

2. Numerical Simulations

We investigate climate responses to a roughness anomaly over an idealized tropical land surface using high-resolution cloud-permitting simulations (Khairoutdinov & Randall, 2003) coupled with a land surface model (Lee & Khairoutdinov, 2015), as detailed in Supporting Information S1. Cloud-permitting simulations are conducted over an idealized limited domain without vegetation, where a roughness anomaly is prescribed, similar to that shown in Figure 1. This idealized setup avoids evaporation differences due to vegetation differences. In addition, soil albedo is independent of soil moisture in our numerical simulations, although albedo changes with soil moisture in the real world (Idso et al., 1975; Rutherford et al., 2017). This setup is used to avoid the additional complexity due to soil albedo differences. In our simulations, the domain is centered at 8°N, and is $25 \times 25 \times 22$ km (Figure S1 in Supporting Information S1) in the x, y (horizontal) and z (vertical) directions, respectively. The domain is horizontally periodic and is divided into two equal patches with different roughness lengths in the x direction (Figure S1 in Supporting Information S1). The patch with the smaller roughness length has a value of $z_0 = 0.0387$ m. The equivalent value for the rougher patch is a multiple of this value, and varies between experiments. For example, rough_1_5 denotes the experiment where the roughness length in the rougher patch is $5z_0$. The prescribed spatial resolution is 250 m in the horizontal direction. The vertical resolution is 30 m (200 m) near the surface (top). The simulations start on January 1 and were run for 500 days. Further descriptions of the land surface model and the cloud-permitting model are available in Supporting Information S1 and previous studies (Cheng et al., 2021; Khairoutdinov & Randall, 2003; Kiehl et al., 1998; Lee & Khairoutdinov, 2015).

We apply the weak-temperature gradient (WTG) approximation (Abbott & Cronin, 2021; Anber et al., 2015; Raymond & Zeng, 2005; Sobel et al., 2001) to model the interaction between convection and large-scale forcing over an idealized tropical land surface. Cloud-permitting models coupled with the WTG approximation have been shown to reasonably simulate temporal variations of precipitation in the Amazon region (Anber et al., 2015). Our results are not qualitatively sensitive to the choice of atmospheric temperature reference profile used in the simulations (Supporting Information S1). The list of experiments prescribed with different roughness anomalies and initial soil moisture are available in Table S1 in Supporting Information S1. For each roughness anomaly experiment, simulations prescribed with different initial soil moisture constitute an ensemble. Surface roughness is characterized by the roughness length z_0. The largest roughness length is $1000z_0 = 38.7$ m. This is not unrealistic since the roughness length can be of the order of $0.1h$ (Leonardi & Castro, 2010; Macdonald et al., 1998; Placidi & Ganapathisubramani, 2015; Raupach, 1992), where h is the obstacle height. We focus on temporal- and ensemble-averages: $\langle\cdot\rangle$ denotes long-term temporal averaging and overbars ($\bar{\cdot}$) denote ensemble averaging (averaging across simulations prescribed with various initial soil moisture).

2.1. Surface Flux Anomalies Caused by Roughness Anomalies

A high roughnesss anomaly causes positive anomalies in both sensible and latent heat fluxes. Over a typical land surface, $H > 0$ and $T_s > T_a$ (outside high latitudes and night), where T_s is the land surface temperature. Introducing a high roughness anomaly increases turbulent mixing near the surface over the roughness anomaly, causing the temperature profile to become more uniform; thus $T_s - T_a$ decreases over the high roughness anomaly. This

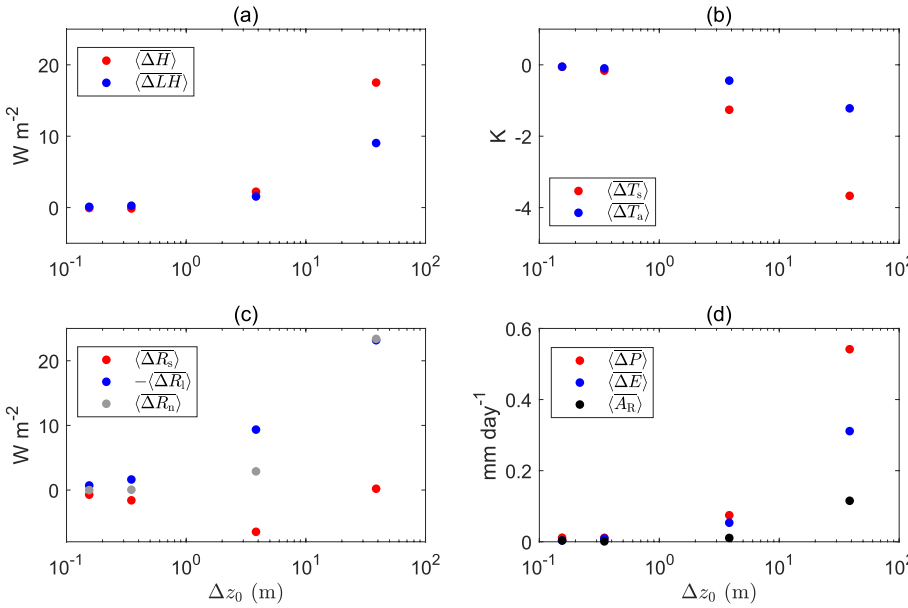

Figure 2. (a) The sensible heat flux anomaly $\langle\overline{\Delta H}\rangle$ and latent heat flux anomaly $\langle\overline{\Delta LH}\rangle$ plotted against the roughness anomaly (Δz_0). (b) Soil temperature anomaly $\langle\overline{\Delta T_s}\rangle$ and near-surface air temperature (15 m above the ground) anomaly $\langle\overline{\Delta T_a}\rangle$ plotted against Δz_0. (c) $\langle\overline{\Delta R_s}\rangle$ (shortwave radiation anomaly), $\langle\overline{\Delta R_l}\rangle$ (longwave radiation anomaly) and $\langle\overline{\Delta R_n}\rangle$ (net radiation anomaly) plotted against Δz_0. At largest Δz_0 of figure (c), the blue dot is covered by the gray dot, since the values represented by these dots are almost the same. (d) The precipitation anomaly $\langle\overline{\Delta P}\rangle$, evaporation anomaly $\langle\overline{\Delta E}\rangle$, and the horizontal convergence (net advection) of moisture into the atmosphere above the high-roughness anomaly $\left(\langle\overline{A_R}\rangle\right)$ plotted against Δz_0.

implies that T_s decreases and/or T_a increases. However, the atmosphere is well-mixed relative to the land surface, so T_a is less sensitive to changes in surface properties than T_s; thus, T_s robustly decreases over the high roughness anomaly. The decline in T_s over the high roughness anomaly causes a decline in outgoing longwave radiation from the surface. This means net radiation is greater over the high roughness anomaly, and so both sensible and latent heat fluxes are also greater over the high roughness anomaly.

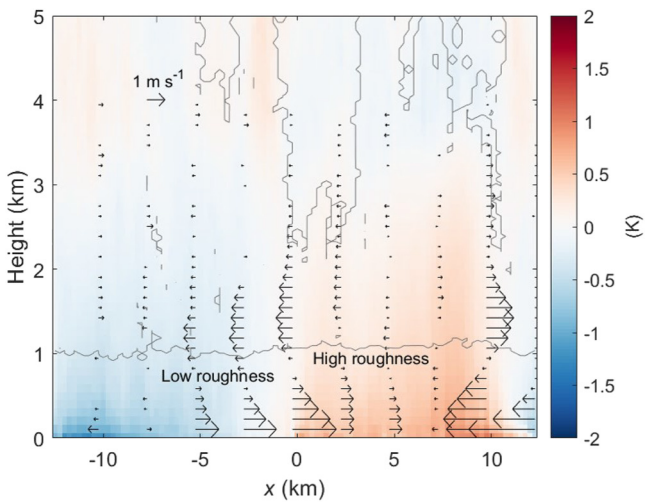

Figure 3. Presence of mesoscale circulations in numerical simulations. *x*-*z* diagram at 1:30 p.m. local time of *y*-averaged quantities for the experiment rough_1_100 on day 500. The color contours denote temperature anomaly. The black arrows denote zonal velocity fluctuation, that is, the difference between zonal velocity and its mean at each height. Note that the zonal velocity fluctuation is only presented for those with a magnitude not less than 0.1 m s^{-1}. The arrow below "1 m s^{-1}" in the figure is not a real velocity but just used as a reference velocity scale. The gray isolines denote non-precipitating cloud ice and water equal to 10^{-5} g kg^{-1}. The *x* axis denotes the distance from domain center in *x* direction.

This mechanism is supported by our simulations. As expected, the high roughness anomaly reduces T_s in our simulations. Specifically, as the prescribed roughness anomaly increases, $\langle\overline{\Delta T_s}\rangle \equiv \langle\overline{T_{s,R} - T_{s,S}}\rangle$ decreases, with $\langle\overline{\Delta T_s}\rangle$ decreasing more than $\langle\overline{\Delta T_a}\rangle$ (Figure 2b). This causes outgoing longwave radiation to decline over the high roughness anomaly, where land surface temperature is lower, resulting in greater net radiation (Figure 2c). Both sensible and latent heat flux anomalies increase with increasing roughness anomaly, consistent with increasing surface net radiation (Figure 2a).

2.2. Thermally Direct Mesoscale Circulations Driven by Surface Flux Anomalies

The resulting sensible heat flux anomalies cause thermally direct mesoscale circulations to form. An example is shown in Figure 3. At 1:30 p.m. local time on day 500 of experiment rough_1_100, the sensible heat flux over the high-roughness anomaly is about 68 W m^{-2} larger than that over the low-roughness background (Figure 3), leading to a transient air temperature anomaly of +1.3 K near the surface. A thermally direct mesoscale circulation is then generated by a pressure anomaly around 12 Pa near the surface due to the temperature anomaly. This thermally direct mesoscale circulation leads to precipitation preferentially over the high-roughness anomaly. The zonal velocity fluctuation (Figure 3), which is the difference between zonal

velocity and its mean at each height, clearly indicates horizontal convergence near the surface and divergence above 1 km over the high-roughness anomaly, consistent with a mesoscale circulation driven by the prescribed roughness anomaly.

The higher air temperatures over the high-roughness anomaly in Figure 3 may appear to contradict the finding that air temperatures are lower, on average, over the roughness anomaly (Figure 2b). The difference is explained by the diurnal cycle. The transiently positive $\langle \overline{\Delta T_a} \rangle$ shown in Figure 3 coincides with the diurnal peak in $\langle \overline{\Delta H} \rangle$ (Figures S3 and S4 in Supporting Information S1). Thus, the anomalously high sensible heat flux over the roughness anomaly causes air temperatures to transiently rise during the day, which triggers mesoscale circulations. But, the transient increase in air temperatures quickly recedes, resulting in lower air temperatures over the high-roughness anomaly, on average.

The mesoscale circulations trigger uplift and greater precipitation over the high-roughness anomaly (positive $\langle \overline{\Delta P} \rangle$, Figure 2d). Net advection of moisture into the high-roughness anomaly (positive $\langle \overline{A_R} \rangle$, Figure 2d) is consistent with this mechanism. The high precipitation anomaly only occurs when the atmosphere is sufficiently wet (Figure S6d in Supporting Information S1).

3. Summary and Discussion

We report thermally direct mesoscale circulations driven by a land surface roughness anomaly. The mechanism promotes precipitation over high roughness anomalies at mesoscales. To our knowledge, this mechanism is new, and is distinct from "dynamically driven" mechanisms reported in previous studies (Khanna & Medvigy, 2014; Samuelsson & Tjernström, 2001). Although the effects of land surface heterogeneities on climate have been studied in terms of deforestation (Khanna & Medvigy, 2014; Khanna et al., 2017; Winckler et al., 2019), urbanization (Li et al., 2021; Rajeswari et al., 2021; W. Wang, 2009; Zhu et al., 2016), and construction of wind farms (Baidya Roy et al., 2004; Fiedler & Bukovsky, 2011), these studies do not identify the thermally direct mechanism shown here. Studies using coarse-resolution climate models do not resolve mesoscale circulations at all (Davin & de Noblet-Ducoudré, 2010; Dickinson & Henderson-Sellers, 1988; Lean & Warrilow, 1989; Li et al., 2018; C. Wang & Prinn, 2010; Winckler et al., 2019), so higher resolution simulations must be used instead. Of those studies, some include an imposed mean wind, in which the "dynamically driven" mechanism likely dominates and obscures the thermally direct mechanism (Claussen, 1989; Courault et al., 2007; Huang & Margulis, 2009; Khanna & Medvigy, 2014; Li et al., 2021; Lin & Glendening, 2002; Maronga & Raasch, 2013; Miller & Stoll, 2013; Rajeswari et al., 2021; Stoll & Porté-Agel, 2006; Wright et al., 1998). Others do not include an interactive surface energy budget, instead prescribing surface temperatures or surface fluxes, which precludes the mechanism identified here (Claussen, 1989; Huang & Margulis, 2009; Lin & Glendening, 2002; Maronga & Raasch, 2013; Miller & Stoll, 2013; Stoll & Porté-Agel, 2006; W. Wang, 2009; Wright et al., 1998; Zhu et al., 2016). Figure S7 in Supporting Information S1 highlights key differences between our study and previous literature.

Our proposed roughness-anomaly mechanism may moderate warming in urban environments caused by coincident anomalies in surface albedo and vegetation transpiration (Bounoua et al., 2015; Grimmond, 2007). The proposed mechanism predicts that the high roughness anomaly caused by urban areas will enhance turbulent mixing and decrease surface and near-surface temperatures, on average, potentially offsetting some urban heat island effects (Figure 2b).

Our work is subject to limitations. We have deliberately focused on an idealized representation of land surface roughness (z_0) to understand the most essential features of the mechanism. However, an important next step is to quantitatively evaluate the mechanism with more realistic roughness schemes, including parameterizations of forest canopies (Bonan et al., 2018), urban canopies (Santiago & Martilli, 2010) and elevated momentum sinks (Fitch et al., 2013; Wu & Archer, 2021) for forests, cities and wind farms, respectively. Wind farms, in particular, induce important changes in near-surface turbulence that go beyond simple increases in z_0 (Fitch et al., 2013; Wu & Archer, 2021).

For maximum simplicity, our study also does not include a mean wind. It is plausible that a sufficiently large roughness anomaly may obstruct the mean wind flow, decreasing the mean wind speed, and thus decreasing the sensible heat flux anomaly. This dynamical weakening of the sensible heat flux anomaly acts against the proposed thermally direct mechanism proposed here, and should be investigated in future work. In addition,

our study also deliberately treats soil albedo as independent of soil moisture, even though soil albedo typically decreases as soil moisture increases (Idso et al., 1975). In our numerical simulations, the high roughness anomaly leads to a larger sensible heat flux, more precipitation, and higher soil moisture. If the effects of soil moisture on soil albedo are considered, the high roughness anomaly will lead to lower soil albedo, which further strengthens the mechanism proposed here.

A variety of scale-dependent climate responses to the presence of wind farms likely exist, beyond the mechanism presented here (Baidya Roy et al., 2004; Fiedler & Bukovsky, 2011; Fitch et al., 2013; Zhou et al., 2012). Our study focuses on mesoscale roughness heterogeneity (O(10 km)) without considering changes in large-scale forcings. However, a roughness anomaly at larger spatial scales may trigger changes in large-scale forcings and thus lead to different precipitation responses. For example, large-scale urbanization (O(1,000 km)) may influence the summer monsoon system in China (Chen et al., 2016). Conversion of land cover from forest to croplands over the Indian subcontinent and Southeastern China weakens the Asian summer monsoon circulation (Takata et al., 2009). In addition, the precipitation response to continental-scale tropical deforestation depends on the spatial scale (Lawrence & Vandecar, 2015). Nevertheless, this work identifies a basic new mechanism by which wind farms, cities, and forests may trigger storms, by inducing thermally-direct mesoscale circulations solely caused by roughness anomalies.

Data Availability Statement

The dataset used for this study is available for public access on the Harvard dataverse (https://doi.org/10.7910/DVN/R1J7FQ).

Acknowledgments
K.A.M. acknowledges funding from NSF Grant AGS-2129576 and a Sloan Research Fellowship. We thank Dr. Marat Khairoutdinov for providing the models used in this study (SAM and SLM). The computations in this paper were run on the FASRC Cannon cluster supported by the FAS Division of Science Research Computing Group at Harvard University.

References

Abbott, T. H., & Cronin, T. W. (2021). Aerosol invigoration of atmospheric convection through increases in humidity. *Science*, *371*(6524), 83–85. https://doi.org/10.1126/science.abc5181

Anber, U., Gentine, P., Wang, S., & Sobel, A. H. (2015). Fog and rain in the amazon. *Proceedings of the National Academy of Sciences of the United States of America*, *112*(37), 11473–11477. https://doi.org/10.1073/pnas.150507711

Baidya Roy, S., Pacala, S. W., & Walko, R. (2004). Can large wind farms affect local meteorology? *Journal of Geophysical Research*, *109*(D19), D19101. https://doi.org/10.1029/2004JD004763

Bonan, G. B., Patton, E. G., Harman, I. N., Oleson, K. W., Finnigan, J. J., Lu, Y., & Burakowski, E. A. (2018). Modeling canopy-induced turbulence in the Earth system: A unified parameterization of turbulent exchange within plant canopies and the roughness sublayer (CLM-ml v0). *Geoscientific Model Development*, *11*(4), 1467–1496. https://doi.org/10.5194/gmd-11-1467-2018

Bounoua, L., Zhang, P., Mostovoy, G., Thome, K., Masek, J., Imhoff, M., et al. (2015). Impact of urbanization on us surface climate. *Environmental Research Letters*, *10*(8), 084010. https://doi.org/10.1088/1748-9326/10/8/084010

Chen, H., Zhang, Y., Yu, M., Hua, W., Sun, S., Li, X., & Gao, C. (2016). Large-scale urbanization effects on eastern Asian summer monsoon circulation and climate. *Climate Dynamics*, *47*(1–2), 117–136. https://doi.org/10.1007/s00382-015-2827-3

Cheng, Y., Chan, P. W., Wei, X., Hu, Z., Kuang, Z., & McColl, K. A. (2021). Soil moisture control of precipitation re-evaporation over a heterogeneous land surface. *Journal of the Atmospheric Sciences*, *78*(10), 3369–3383. https://doi.org/10.1175/JAS-D-21-0059.1

Claussen, M. (1989). Neutral surface-layer flow over isolated roughness strips. *Boundary-Layer Meteorology*, *48*(4), 431–442. https://doi.org/10.1007/BF00123064

Courault, D., Drobinski, P., Brunet, Y., Lacarrere, P., & Talbot, C. (2007). Impact of surface heterogeneity on a buoyancy-driven convective boundary layer in light winds. *Boundary-Layer Meteorology*, *124*(3), 383–403. https://doi.org/10.1007/s10546-007-9172-y

Davin, E. L., & de Noblet-Ducoudré, N. (2010). Climatic impact of global-scale deforestation: Radiative versus nonradiative processes. *Journal of Climate*, *23*(1), 97–112. https://doi.org/10.1175/2009JCLI3102.1

Deardorff, J. W. (1972). Parameterization of the planetary boundary layer for use in general circulation models. *Monthly Weather Review*, *100*(2), 93–106. https://doi.org/10.1175/1520-0493(1972)100<0093:POTPBL>2.3.CO;2

Dickinson, R. E., & Henderson-Sellers, A. (1988). Modelling tropical deforestation: A study of GCM land-surface parametrizations. *Quarterly Journal of the Royal Meteorological Society*, *114*(480), 439–462. https://doi.org/10.1002/qj.49711448009

Fiedler, B. H., & Bukovsky, M. S. (2011). The effect of a giant wind farm on precipitation in a regional climate model. *Environmental Research Letters*, *6*(4), 045101. https://doi.org/10.1088/1748-9326/6/4/045101

Fitch, A. C., Olson, J. B., & Lundquist, J. K. (2013). Parameterization of wind farms in climate models. *Journal of Climate*, *26*(17), 6439–6458. https://doi.org/10.1175/JCLI-D-12-00376.1

Grimmond, S. (2007). Urbanization and global environmental change: Local effects of urban warming. *The Geographical Journal*, *173*(1), 83–88. https://doi.org/10.1111/j.1475-4959.2007.232_3.x

Huang, H.-Y., & Margulis, S. A. (2009). On the impact of surface heterogeneity on a realistic convective boundary layer. *Water Resources Research*, *45*(4). https://doi.org/10.1029/2008WR007175

Idso, S., Jackson, R., Reginato, R., Kimball, B., & Nakayama, F. (1975). The dependence of bare soil albedo on soil water content. *Journal of Applied Meteorology*, *14*(1), 109–113. https://doi.org/10.1175/1520-0450(1975)014<0109:TDOBSA>2.0.CO;2

Khairoutdinov, M. F., & Randall, D. A. (2003). Cloud resolving modeling of the ARM summer 1997 IOP: Model formulation, results, uncertainties, and sensitivities. *Journal of the Atmospheric Sciences*, *60*(4), 607–625. https://doi.org/10.1175/1520-0469(2003)060<0607:CRMOTA>2.0.CO;2

Khanna, J., & Medvigy, D. (2014). Strong control of surface roughness variations on the simulated dry season regional atmospheric response to contemporary deforestation in Rondônia, Brazil. *Journal of Geophysical Research: Atmospheres*, *119*(23), 13–067. https://doi.org/10.1002/2014JD022278

Khanna, J., Medvigy, D., Fueglistaler, S., & Walko, R. (2017). Regional dry-season climate changes due to three decades of Amazonian deforestation. *Nature Climate Change*, *7*(3), 200–204. https://doi.org/10.1038/nclimate3226

Kiehl, J., Hack, J., Bonan, G., Boville, B., Williamson, D., & Rasch, P. (1998). The national center for atmospheric research community climate model: CCM3. *Journal of Climate*, *11*(6), 1131–1149. https://doi.org/10.1175/1520-0442(1998)011<1131:TNCFAR>2.0.CO;2

Kirk-Davidoff, D. B., & Keith, D. W. (2008). On the climate impact of surface roughness anomalies. *Journal of the Atmospheric Sciences*, *65*(7), 2215–2234. https://doi.org/10.1175/2007JAS2509.1

Lawrence, D., & Vandecar, K. (2015). Effects of tropical deforestation on climate and agriculture. *Nature Climate Change*, *5*(1), 27–36. https://doi.org/10.1038/nclimate2430

Lean, J., & Warrilow, D. A. (1989). Simulation of the regional climatic impact of amazon deforestation. *Nature*, *342*(6248), 411–413. https://doi.org/10.1038/342411a0

Lee, J. M., & Khairoutdinov, M. (2015). A simplified land model (SLM) for use in cloud-resolving models: Formulation and evaluation. *Journal of Advances in Modeling Earth Systems*, *7*(3), 1368–1392. https://doi.org/10.1002/2014MS000419

Leonardi, S., & Castro, I. P. (2010). Channel flow over large cube roughness: A direct numerical simulation study. *Journal of Fluid Mechanics*, *651*, 519–539. https://doi.org/10.1017/S002211200999423X

Li, Y., Kalnay, E., Motesharrei, S., Rivas, J., Kucharski, F., Kirk-Davidoff, D., et al. (2018). Climate model shows large-scale wind and solar farms in the Sahara increase rain and vegetation. *Science*, *361*(6406), 1019–1022. https://doi.org/10.1126/science.aar5629

Li, Y., Wang, W., Chang, M., & Wang, X. (2021). Impacts of urbanization on extreme precipitation in the Guangdong-Hong Kong-Macau greater bay area. *Urban Climate*, *38*, 100904. https://doi.org/10.1016/j.uclim.2021.100904

Lin, C.-L., & Glendening, J. W. (2002). Large eddy simulation of an inhomogeneous atmospheric boundary layer under neutral conditions. *Journal of the Atmospheric Sciences*, *59*(16), 2479–2497. https://doi.org/10.1175/1520-0469(2002)059<2479:LESOAI>2.0.CO;2

Louis, J.-F. (1979). A parametric model of vertical eddy fluxes in the atmosphere. *Boundary-Layer Meteorology*, *17*(2), 187–202. https://doi.org/10.1007/BF00117978

Macdonald, R., Griffiths, R., & Hall, D. (1998). An improved method for the estimation of surface roughness of obstacle arrays. *Atmospheric Environment*, *32*(11), 1857–1864. https://doi.org/10.1016/S1352-2310(97)00403-2

Maronga, B., & Raasch, S. (2013). Large-eddy simulations of surface heterogeneity effects on the convective boundary layer during the LITFASS-2003 experiment. *Boundary-Layer Meteorology*, *146*(1), 17–44. https://doi.org/10.1007/s10546-012-9748-z

Miller, N. E., & Stoll, R. (2013). Surface heterogeneity effects on regional-scale fluxes in the stable boundary layer: Aerodynamic roughness length transitions. *Boundary-Layer Meteorology*, *149*(2), 277–301. https://doi.org/10.1007/s10546-013-9839-5

Placidi, M., & Ganapathisubramani, B. (2015). Effects of frontal and plan solidities on aerodynamic parameters and the roughness sublayer in turbulent boundary layers. *Journal of Fluid Mechanics*, *782*, 541–566. https://doi.org/10.1017/jfm.2015.552

Rajeswari, J., Srinivas, C., Yesubabu, V., Hari Prasad, D., & Venkatraman, B. (2021). Impacts of urbanization, aerodynamic roughness, and land surface processes on the extreme heavy rainfall over Chennai, India. *Journal of Geophysical Research: Atmospheres*, *126*(10), e2020JD034017. https://doi.org/10.1029/2020JD034017

Raupach, M. (1992). Drag and drag partition on rough surfaces. *Boundary-Layer Meteorology*, *60*(4), 375–395. https://doi.org/10.1007/BF00155203

Raymond, D. J., & Zeng, X. (2005). Modelling tropical atmospheric convection in the context of the weak temperature gradient approximation. *Quarterly Journal of the Royal Meteorological Society*, *131*(608), 1301–1320. https://doi.org/10.1256/qj.03.97

Rutherford, W. A., Painter, T. H., Ferrenberg, S., Belnap, J., Okin, G. S., Flagg, C., & Reed, S. C. (2017). Albedo feedbacks to future climate via climate change impacts on dryland biocrusts. *Scientific Reports*, *7*(1), 1–9. https://doi.org/10.1038/srep44188

Samuelsson, P., & Tjernström, M. (2001). Mesoscale flow modification induced by land-lake surface temperature and roughness differences. *Journal of Geophysical Research*, *106*(D12), 12419–12435. https://doi.org/10.1029/2001JD900057

Santiago, J., & Martilli, A. (2010). A dynamic urban canopy parameterization for mesoscale models based on computational fluid dynamics Reynolds-averaged Navier–Stokes microscale simulations. *Boundary-Layer Meteorology*, *137*(3), 417–439. https://doi.org/10.1007/s10546-010-9538-4

Sobel, A. H., Nilsson, J., & Polvani, L. M. (2001). The weak temperature gradient approximation and balanced tropical moisture waves. *Journal of the Atmospheric Sciences*, *58*(23), 3650–3665. https://doi.org/10.1175/1520-0469(2001)058<3650:TWTGAA>2.0.CO;2

Stoll, R., & Porté-Agel, F. (2006). Effect of roughness on surface boundary conditions for large-eddy simulation. *Boundary-Layer Meteorology*, *118*(1), 169–187. https://doi.org/10.1007/s10546-005-4735-2

Takata, K., Saito, K., & Yasunari, T. (2009). Changes in the Asian monsoon climate during 1700–1850 induced by preindustrial cultivation. *Proceedings of the National Academy of Sciences of the United States of America*, *106*(24), 9586–9589. https://doi.org/10.1073/pnas.080734610

Wang, C., & Prinn, R. G. (2010). Potential climatic impacts and reliability of very large-scale wind farms. *Atmospheric Chemistry and Physics*, *10*(4), 2053–2061. https://doi.org/10.5194/acp-10-2053-2010

Wang, W. (2009). The influence of thermally-induced mesoscale circulations on turbulence statistics over an idealized urban area under a zero background wind. *Boundary-Layer Meteorology*, *131*(3), 403–423. https://doi.org/10.1007/s10546-009-9378-2

Winckler, J., Reick, C. H., Bright, R. M., & Pongratz, J. (2019). Importance of surface roughness for the local biogeophysical effects of deforestation. *Journal of Geophysical Research: Atmospheres*, *124*(15), 8605–8618. https://doi.org/10.1029/2018JD030127

Wright, S., Elliott, L., Ingham, D. B., & Hewson, M. J. C. (1998). The adaptation of the atmospheric boundary layer to a change in surface roughness. *Boundary-Layer Meteorology*, *89*(2), 175–195. https://doi.org/10.1023/A:1001729107562

Wu, S., & Archer, C. L. (2021). Near-ground effects of wind turbines: Observations and physical mechanisms. *Monthly Weather Review*, *149*(3), 879–898. https://doi.org/10.1175/MWR-D-20-0186.1

Zhou, L., Tian, Y., Baidya Roy, S., Thorncroft, C., Bosart, L. F., & Hu, Y. (2012). Impacts of wind farms on land surface temperature. *Nature Climate Change*, *2*(7), 539–543. https://doi.org/10.1038/nclimate1505

Zhu, X., Ni, G., Cong, Z., Sun, T., & Li, D. (2016). Impacts of surface heterogeneity on dry planetary boundary layers in an urban-rural setting. *Journal of Geophysical Research: Atmospheres*, *121*(20), 12–164. https://doi.org/10.1002/2016JD024982

Thermally direct mesoscale circulations caused by land surface roughness gradients

Yu Cheng[1], **Kaighin A. McColl**[1,2]

[1]Department of Earth and Planetary Sciences, Harvard University, Cambridge, Massachusetts, USA
[2]School of Engineering and Applied Sciences, Harvard University, Cambridge, Massachusetts, USA

Contents of this file

1 Supplementary Materials

1.1 Idealized illustration of the mechanism

Consider a deliberately extreme, idealized example, used here to qualitatively illustrate differential heating caused by roughness anomalies. An otherwise uniform domain is divided into two regions, one very rough (denoted with 'R' subscripts) and one very smooth (denoted with 'S' subscripts). In this idealized example, the roughness of the surface entirely controls the intensity of turbulent mixing near the surface, encoded in the 'aerodynamic conductance' parameter (g_a), implying that $g_{\mathrm{a,\,S}}$ is very small and $g_{\mathrm{a,\,R}}$ is very large. For simplicity, consider the limiting case in which $g_{\mathrm{a,\,S}} \to 0$ and $g_{\mathrm{a,\,R}} \to \infty$. For a zero heat capacity land surface, the surface energy balance is

$$(1-\alpha)R_{\mathrm{s,\,d}} + R_{\mathrm{l,\,d}} - \epsilon\sigma T_\mathrm{s}^4 = \overbrace{\rho c_\mathrm{p} g_\mathrm{a}(T_\mathrm{s} - T_\mathrm{a})}^{\equiv H} + \overbrace{\rho L_\mathrm{v} \frac{g_\mathrm{s} g_\mathrm{a}}{g_\mathrm{s} + g_\mathrm{a}}(q^*(T_\mathrm{s}) - q_\mathrm{a})}^{\equiv LH}, \tag{S1}$$

where α is surface albedo, $R_{\mathrm{s,\,d}}$ downwelling shortwave radiation at the surface, $R_{\mathrm{l,\,d}}$ downwelling longwave radiation at the surface, ϵ the surface emissivity, σ the Stefan-Boltzmann constant, T_s the land surface temperature, ρ the air density, c_p the specific heat capacity of air at constant pressure, T_a the air temperature at a reference height, L_v the latent heat of vaporization, H the sensible heat flux, LH the latent heat flux, g_s the surface conductance characterizing the limitations due to water availability, q^* the saturation specific humidity, and q_a the specific humidity at the reference height. In our idealized example, the near-surface temperature and humidity are both fixed values, as are the net downwelling radiative fluxes.

Limits of the surface energy balance (corresponding to $g_{\mathrm{a,\,S}} \to 0$ and $g_{\mathrm{a,\,R}} \to \infty$) are presented in detail elsewhere (McColl, 2020), but are briefly reviewed here. In the limit $g_\mathrm{a} \to 0$, the turbulent fluxes on the right hand side approach zero; the surface energy balance is maintained by causing $T_s \to (((1-\alpha)R_{\mathrm{s,\,d}} + R_{\mathrm{l,\,d}})/(\epsilon\sigma))^{1/4}$. Thus, in our idealized example, $H_\mathrm{S} = 0$ and the near-surface atmosphere is not heated by the land surface (the heating of near-surface air by the net emission of longwave radiation from the surface is much smaller than the heating associated with sensible heat flux, since radiative heating is distributed throughout the atmosphere, whereas sensible heating is concentrated at the surface).

Corresponding author: Kaighin A. McColl, kmccoll@seas.harvard.edu

In the limit $g_a \to \infty$, to maintain surface energy balance, it is required that $T_s \to T_a$. This implies that

$$H_R = \lim_{g_a \to \infty} H = (1-\alpha)R_{s,\,d} + R_{l,\,d} - \epsilon\sigma T_a^4 - \rho L_v g_s(q^*(T_a) - q_a). \tag{S2}$$

Combining these results for H_R and H_S yields Equation 1.

1.2 Numerical simulations

In our numerical simulations, the System for Atmospheric Modeling (SAM; version 6.11.1) described in Khairoutdinov and Randall (2003) is coupled with a land surface model (Lee & Khairoutdinov, 2015). To compute longwave and shortwave radiation, the National Center for Atmospheric Research (NCAR) Community Climate Model (CCM3) is used (Kiehl et al., 1998). The 1.5-order closure subgrid-scale (SGS) model consists of a prognostic SGS turbulent kinetic energy (Khairoutdinov & Randall, 2003). To predict the mixing ratios of hydrometeor species, a single-moment microphysics scheme (SAM1MOM) is used (Khairoutdinov & Randall, 2003). To compute atmospheric surface fluxes in the land surface model, we solve standard energy and moisture balance equations (Lee & Khairoutdinov, 2015).

We apply the weak-temperature gradient (WTG) approximation (Sobel et al., 2001) to model the interaction between convection and large-scale forcing (Raymond & Zeng, 2005), a scheme that is most applicable to a tropical environment. The WTG scheme introduced by Raymond and Zeng (2005) is applied, where the mean temperature profile is relaxed toward a reference profile by adding an advection term caused by a hypothetical vertical velocity. Detailed descriptions of the WTG scheme are provided in previous studies (Raymond & Zeng, 2005; Abbott & Cronin, 2021). To compute the WTG vertical velocity, we use the same parameters as those in Abbott and Cronin (2021). We apply the output of a radiative-convective equilibrium simulation over a tropical ocean in Abbott and Cronin (2021) as the reference temperature profile. The WTG reference profile used in the main text leads to high relative humidity (around 88%) near the surface (Fig. S5). To investigate the sensitivity of our results to the choice of the imposed reference temperature profile, we conduct additional numerical simulations through modifying the WTG reference profile used in the main text to obtain drier conditions. According to Anber et al. (2015), potential temperature near the surface (below approximately 800 hPa) from wetter reference profiles (that lead to more precipitation) is lower than that from the drier reference profiles (that lead to less precipitation). In addition, potential temperature above 400 hPa from the wetter reference profiles is higher than that from the drier reference profiles (Anber et al., 2015). We therefore conducted 8 additional simulations in which the reference profile used in experiments listed in Table S1 was modified for the experiment rough_1_1000 ($\phi_{ini} = 10\%$) to obtain less precipitation, mainly through increasing temperatures approximately below 4 km and decreasing temperatures approximately between 4 km and 16 km as shown in Fig. S5. These sensitivity studies confirmed that our results are not qualitatively sensitive to the choice of atmospheric profile used in the WTG simulations (Fig. S6).

The daily precipitation averaged over both the whole domain (P_M) and the high-roughness patch (P_R) approaches a quasi-steady state after 10 days (Fig. S2). Due to computational storage limits, the climate variables during the 500-day simulations were averaged every 12 hours, and the average over 500 days was used as the long-term averaging in the main text. To obtain hourly climate variables, the simulations were run for an additional 50 days, where the variables were analyzed in Figures S3 and S4. The simulations include a diurnal cycle, but do not include a seasonal cycle. In Table S1, the list of experiments with different roughness gradients and initial soil moisture values are described.

1.3 Estimation of moisture advection from column water anomaly budgets

The budgets of total atmospheric moisture over each subdomain are used to compute the moisture advection between the two patches prescribed with different roughness lengths. The moisture balance equation for a control volume over the high-roughness patch can be written as

$$\frac{\partial W_{\mathrm{R}}}{\partial t} = E_{\mathrm{R}} - P_{\mathrm{R}} + A_{\mathrm{R}} + S_{\mathrm{WTG}}, \tag{S3}$$

where W_{R} (unit in mm) is column-integrated total moisture including vapor, liquid and solid water in the air over the high-roughness patch, E_{R} (unit in mm day^{-1}) and P_{R} (unit in mm day^{-1}) are averaged evaporation and precipitation rates over the high-roughness patch, respectively, A_{R} (unit in mm day^{-1}) is the net horizontal convergence (net advection) of moisture into the high-roughness patch, and S_{WTG} (unit in mm day^{-1}) is the source term due to the WTG approximation. Similarly, the moisture balance equation for the low-roughness patch can be written as

$$\frac{\partial W_{\mathrm{S}}}{\partial t} = E_{\mathrm{S}} - P_{\mathrm{S}} + A_{\mathrm{S}} + S_{\mathrm{WTG}}. \tag{S4}$$

As the domain is divided into two patches, we have

$$A_{\mathrm{R}} = -A_{\mathrm{S}}. \tag{S5}$$

We compute daily averaged A_{R} and S_{WTG} based on Equations S3-S5.

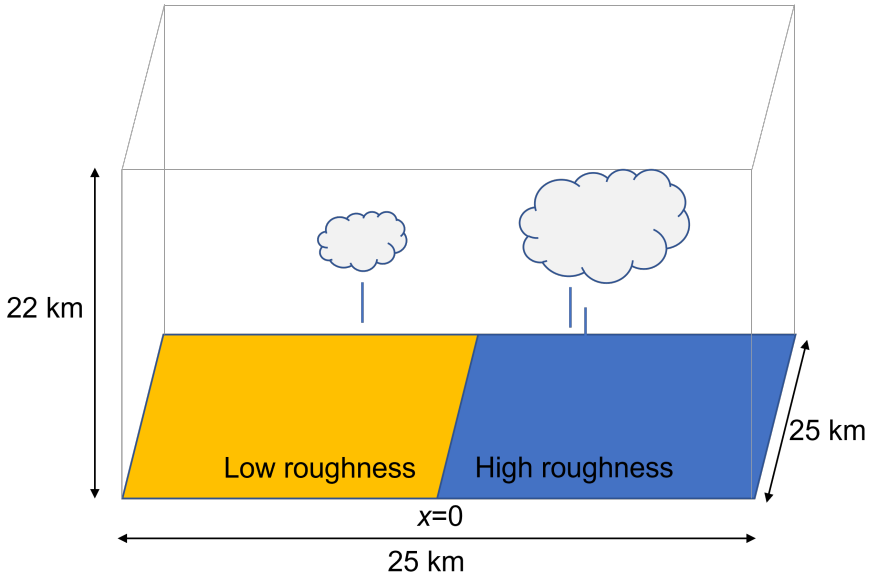

Figure S1. Schematic of roughness setup in the computational domain.

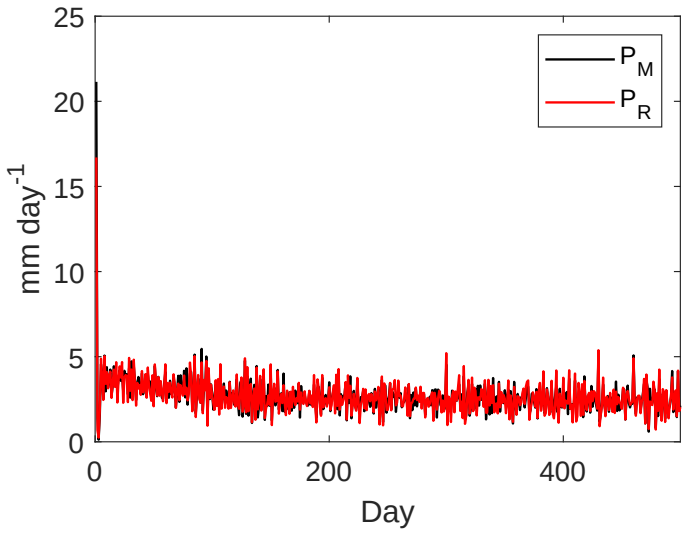

Figure S2. Temporal series of daily precipitation averaged over the whole domain (P_{M}) and over the high-roughness patch (P_{R}) in the experiment rough_1_5 where $\phi_{\mathrm{ini}} = 0.1$.

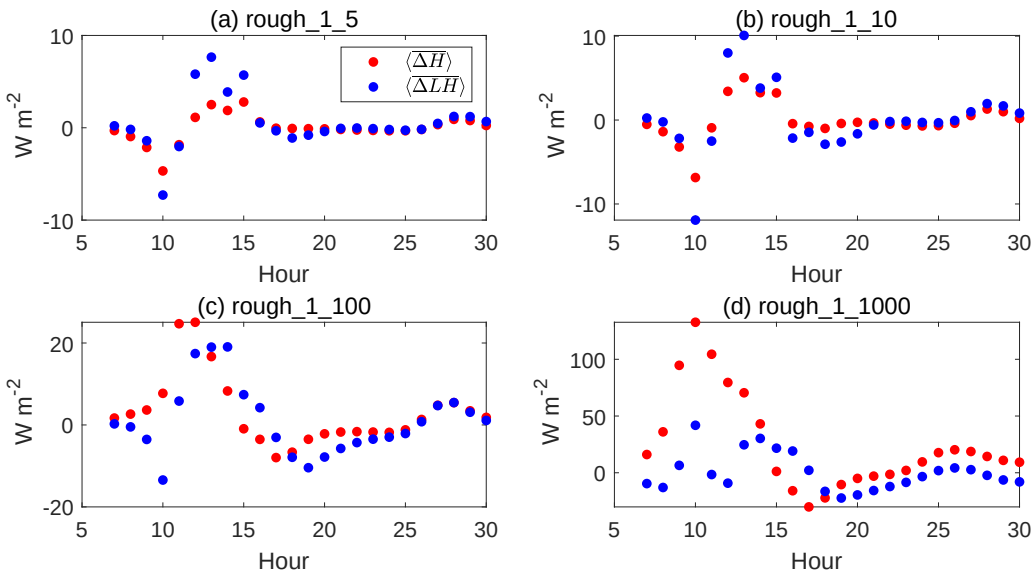

Figure S3. Diurnal cycle of the sensible heat flux anomaly $\langle\overline{\Delta H}\rangle$ and latent heat flux anomaly $\langle\overline{\Delta LH}\rangle$ averaged in Days 500-550 in the experiments rough_1_5, rough_1_10 , rough_1_100, and rough_1_1000.

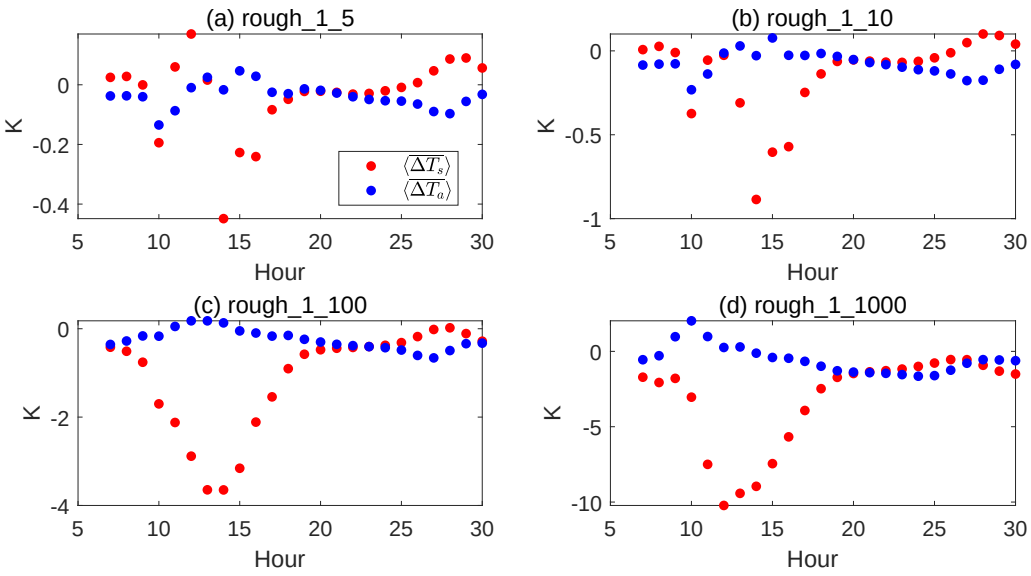

Figure S4. Diurnal cycle of the land surface temperature anomaly $\langle\overline{\Delta T_s}\rangle$ and near-surface air temperature anomaly $\langle\overline{\Delta T_a}\rangle$ averaged in Days 500-550 in the experiments rough_1_5, rough_1_10 , rough_1_100, and rough_1_1000..

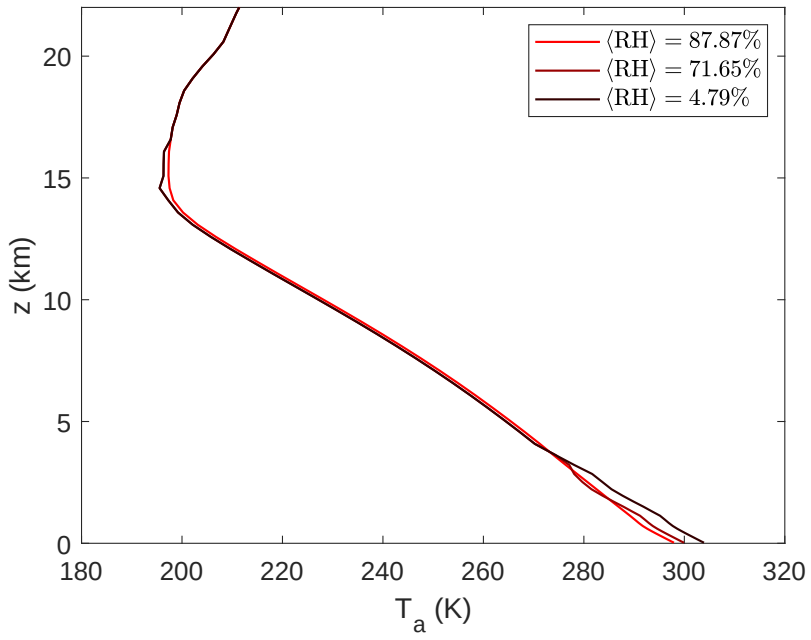

Figure S5. Three example vertical temperature profiles used as the WTG reference profiles in our numerical simulations. In the legend, relative humidity $\langle$RH$\rangle$ at the lowest grid level (15 m above the ground) is shown. The profile denoted by $\langle$RH$\rangle$ = 87.87% is the WTG reference temperature profile used throughout the main text. The other profiles are examples of profiles used in the sensitivity analysis. Eight profiles were used in total, but not all are shown here, since they substantially overlap.

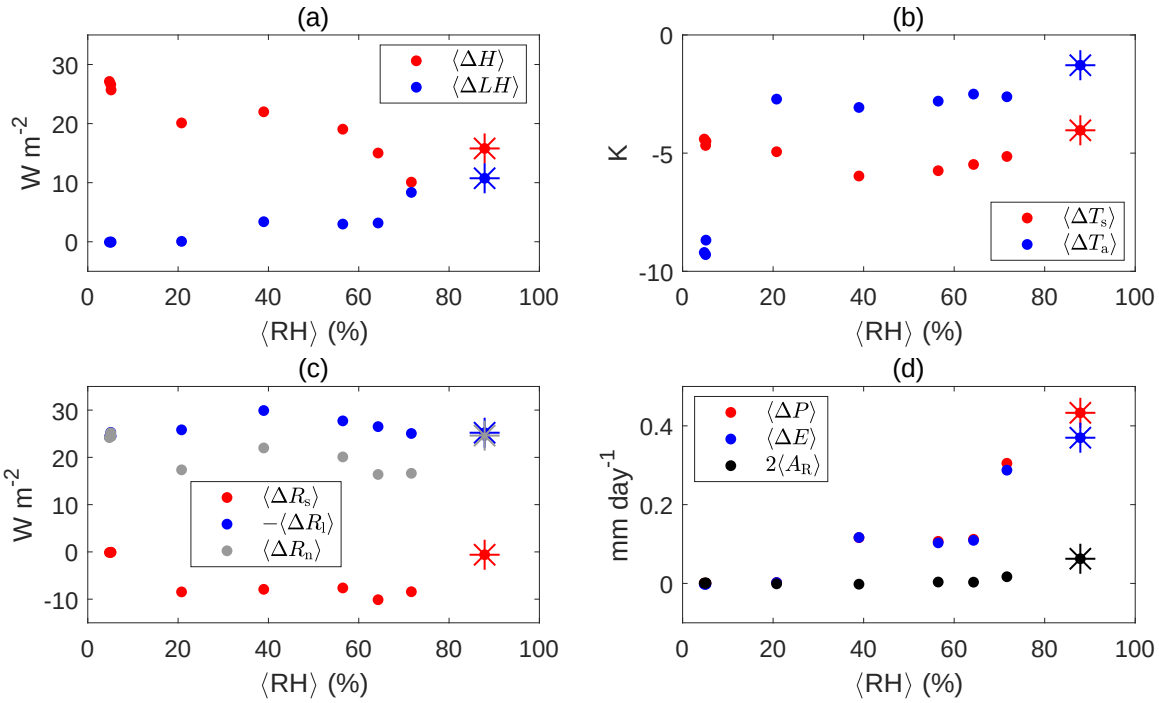

Figure S6. Climate variables from rough_1_1000 simulations using different WTG reference temperature profiles. The variables on the y axis are the same as those in Fig. 2. In the x axis, relative humidity $\langle \mathrm{RH} \rangle$ at the lowest grid level (15 m above the ground) is shown, with different values corresponding to different WTG reference profiles, as in Fig. S5. The asterisks denote climate variables from the experiment where the reference temperature profile is the same as that in Fig. 2.

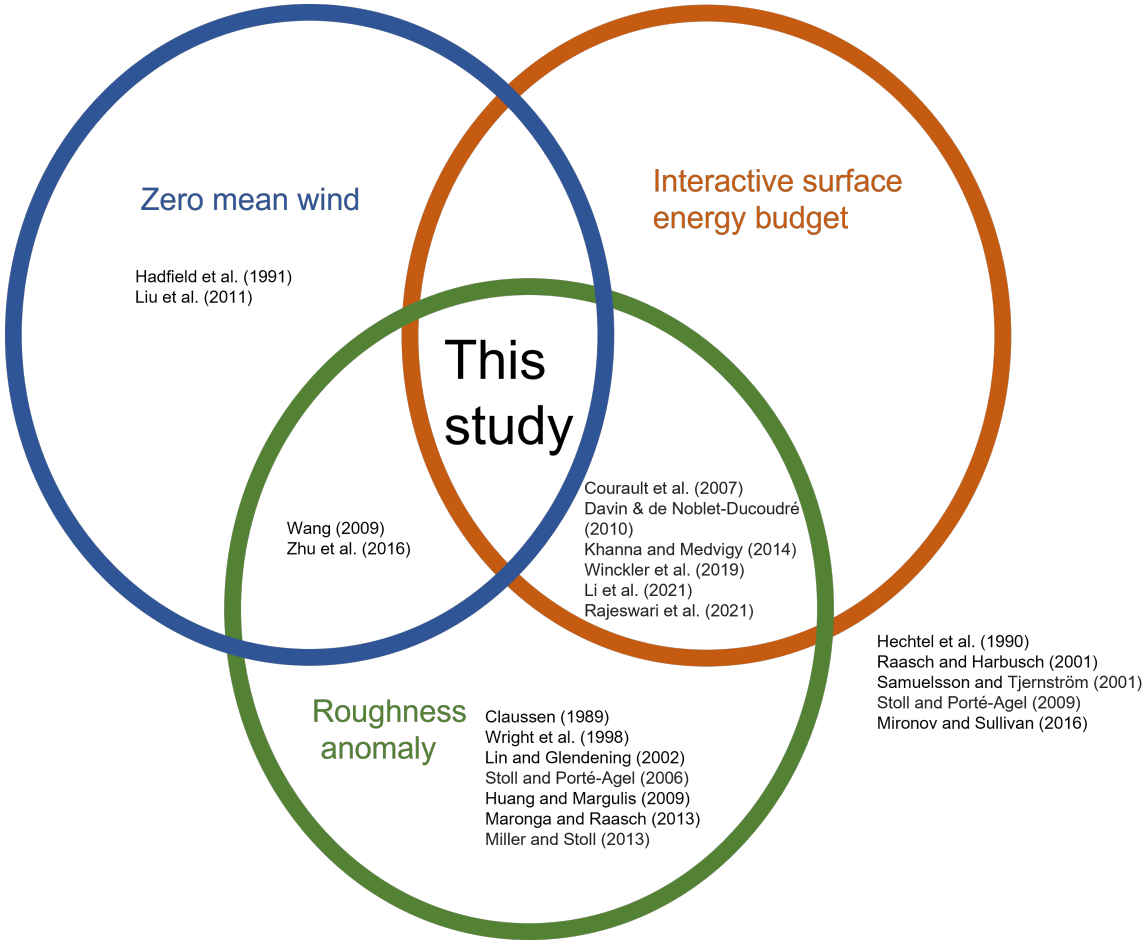

Figure S7. Venn diagram categorizing some relevant previous studies investigating heterogeneous land effects on climate, and their relation to this study.

Table S1. List of experiments run in this study. There are 24 numerical experiments in total. The horizontal resolution is 250 m. The roughness length $z_0 = 0.0387$ m.

Numerical experiments	roughness $z_{0,\mathrm{S}}$	roughness $z_{0,\mathrm{R}}$	Initial soil moisture ϕ_{ini} (%) ($\mathrm{m}^3\ \mathrm{m}^{-3}$)
rough_1_5	z_0	$5z_0$	10 (0.0468), 20 (0.0935), 30 (0.1403), 40 (0.1870), 50 (0.2338), 60 (0.2805),
rough_1_10	z_0	$10z_0$	10 (0.0468), 20 (0.0935), 30 (0.1403), 40 (0.1870), 50 (0.2338), 60 (0.2805),
rough_1_100	z_0	$100z_0$	10 (0.0468), 20 (0.0935), 30 (0.1403), 40 (0.1870), 50 (0.2338), 60 (0.2805)
rough_1_1000	z_0	$1000z_0$	10 (0.0468), 20 (0.0935), 30 (0.1403), 40 (0.1870), 50 (0.2338), 60 (0.2805)

References

Abbott, T. H., & Cronin, T. W. (2021). Aerosol invigoration of atmospheric convection through increases in humidity. *Science*, *371*(6524), 83–85. https://doi.org/10.1126/science.abc5181.

Anber, U., Gentine, P., Wang, S., & Sobel, A. H. (2015). Fog and rain in the amazon. *Proc. Natl. Acad. Sci.*, *112*(37), 11473–11477. https://doi.org/10.1073/pnas.150507711.

Khairoutdinov, M. F., & Randall, D. A. (2003). Cloud resolving modeling of the arm summer 1997 iop: Model formulation, results, uncertainties, and sensitivities. *J. Atmos. Sci.*, *60*(4), 607–625. https://doi.org/10.1175/1520-0469(2003)060<0607:CRMOTA>2.0.CO;2.

Kiehl, J., Hack, J., Bonan, G., Boville, B., Williamson, D., & Rasch, P. (1998). The national center for atmospheric research community climate model: Ccm3. *J. Clim.*, *11*(6), 1131–1149. https://doi.org/10.1175/1520-0442(1998)011<1131:TNCFAR>2.0.CO;2.

Lee, J. M., & Khairoutdinov, M. (2015). A simplified land model (slm) for use in cloud-resolving models: Formulation and evaluation. *J. Adv. Model. Earth Syst.*, *7*(3), 1368–1392. https://doi.org/10.1002/2014MS000419.

McColl, K. A. (2020). Practical and theoretical benefits of an alternative to the penman-monteith evapotranspiration equation. *Water Resources Research*, *56*(6), e2020WR027106. https://doi.org/10.1029/2020WR027106.

Raymond, D. J., & Zeng, X. (2005). Modelling tropical atmospheric convection in the context of the weak temperature gradient approximation. *Quart. J. Roy. Meteor. Soc.*, *131*(608), 1301–1320. https://doi.org/10.1256/qj.03.97.

Sobel, A. H., Nilsson, J., & Polvani, L. M. (2001). The weak temperature gradient approximation and balanced tropical moisture waves. *J. Atmos. Sci.*, *58*(23), 3650–3665. https://doi.org/10.1175/1520-0469(2001)058<3650:TWTGAA>2.0.CO;2.